Dalton Transactions

Accepted Manuscript

ROYAL SOCIETY OF CHEMISTRY

www.rsc.org/dalton

Journal Name

RSCPublishing

ARTICLE

Crystal Chemical Characteristics of Ellestadite-type Apatite: Implications for Toxic Metal Immobilization

Cite this: DOI: 10.1039/x0xx00000x

YN Fang*[a,b] Clemens Ritter[c] and T. J. White*[a,b]

Received 00th January 2012,
Accepted 00th January 2012

DOI: 10.1039/x0xx00000x

www.rsc.org/

The ellestadite apatites $Ca_{10}[(SiO_4)_x(PO_4)_{6-2x}(SO_4)_x]Cl_2$ were studied by powder X-ray and neutron diffraction to establish baseline crystallographic data. These synthetic materials, unlike mineral specimens that are well equilibrated, show no Si/P/S ordering and conform to $P6_3/m$ symmetry. Phosphate-rich ellestadites where $0 \leq x \leq 1$ show chemical stability towards Toxicity Characterization Leaching Procedure (TCLP) testing and are potential immobilization matrices for mixed toxic metal wastes.

1 Introduction

The crystal chemical adaptability[1] of apatites make them key materials in a range of technologies deployed for environmental remediation[2], catalysis and energy production, as well as in the traditional biomedical use for bone and teeth replacement. However, the structure of apatite is relatively complex, and optimisation of chemically-substituted apatites for these applications demands a comprehensive understanding of their nanometric chemical and structural properties. Chlorapatite is potentially a host material for the immobilization of chloride contaminated actinide waste[3], and chlorellestadites, synthesized from industrial wastes, show promise as waste form ceramics for the immobilisation of incinerator fly ash containing chlorides, sulphates and heavy metals[4]. However, our crystallochemical knowledge is presently insufficient to tailor ellestadites formulations and reliably predict their durability.

Ellestadites are members of the apatite family represented by the simplified formula $A_{10}(BO_4)_6X_2$ (A = Ca, B = Si/P/S, and X = F, Cl and OH), with substitution of phosphate by silicate and sulphate ($2PO_4^{3-} \rightarrow SiO_4^{4-} + SO_4^{2-}$). Topographically, ellestadites can be described as a $A_4(BO_4)_6$ framework that encloses one dimensional tunnels containing an A_6X_2 component (Fig. 1). The diameter of the tunnel can be adjusted by changing the twist angle of AO_6 metaprisms. The mineral prototype ellestadite from Crestmore, California, with the space group of $P6_3/m$ (space group 176) was first described by McConnell[5]. Pliego-Cuerve and Glasser[6] synthesized $Ca_{10}(SiO_4)_3(SO_4)_3Cl_2$, but did not investigate the crystal chemistry while X-ray data of pure chloride ellestadites (Ca, Pb and Sr) were presented by Neubauer and Pöllmann[7]. The synthetic compounds are all hexagonal $P6_3/m$. A single crystal X-ray diffraction study of a mineral from Chichibu Mine was monoclinic $P2_1/m$ (a = 9.476(2), b = 9.508(2), c = 6.919(1)Å, and γ = 119.53(2)°) and showed the differentiated substitution of SO_4 and SiO_4 for PO_4 groups.[8] This ordering was incomplete and the presence of trace elements prevented deriving an unambiguous solution. This monoclinic cell is distinct from the $P2_1/b$ symmetry (space group 14) of chlorapatite[9], $Ca_{10}(PO_4)_6Cl_2$, where $b = 2a$ and $\gamma = 120°$, due to inter-tunnel ordering of the chlorine atomic columns. Another study of mineral ellestadite found $P2_1$ (space group 4) symmetry which yields three independent $(Si/P/S)O_4$ tetrahedral sites and two independent CaO_6 metaprisms.[10] Thus, the precise arrangement of the metalloids in natural ellestadite and its symmetry remain in question, as does the relevance of these varieties to synthetic ellestadites proposed as immobilization matrices, where crystallization is relatively rapid, and B-site order correlation may be less complete.

The goal of this work was to synthesize a chloroapatite-chlorellestadite solid solution series to serve as a model structure for the incorporation of toxic metals, investigate its crystallochemical properties as a function of the P:(Si/S) ratio, and gather preliminary leaching data.

2 Experimental Methods

2.1 Synthesis

Ellestadites of composition $Ca_{10}[(SiO_4)_x(PO_4)_{6-2x}(SO_4)_x]Cl_2$ were prepared by a solid-state method where the nominal overall reaction was:

$$2x\,CaO + CaCl_2 + x\,SiO_2 + x\,CaSO_4 + (3-x)Ca_3(PO_4)_2 \rightarrow Ca_{10}[(SiO_4)_x(PO_4)_{6-2x}(SO_4)_x]Cl_2 \quad (1)$$

Fresh CaO (prepared by firing Analytical Reagent grade $CaCO_3$ at 900 °C), $CaSO_4$, SiO_2, $Ca_3(PO_4)_2$ and $CaCl_2$ powders were mixed in stoichiometric amounts. After grinding in acetone and drying, the mixtures were fired (950 °C/air/9 hour) in alumina crucibles covered by an alumina slide to slow chlorine volatilization.

2.2 Chemical Analysis

The chemical composition of the ellestadites were determined by electron probe microanalysis (EPMA) using a JEOL JXA-8200 operated at 20 kV, with a beam current of 20 nA, beam diameter of 2.5 μm and peak counting times of 40 second for all elements (both peak and background). The standards used were quartz (Si), a natural apatite (P and Ca), pyrrhotite (S) and NaCl (Cl). Chlorine is always underestimated due to electron beam induced anisotropic diffusion of chlorine along the ellestadite c-axis and volatilization[11].

2.3 Structural characterization

Powder X-ray diffraction (PXRD) data were collected with a Shimadzu Lab XRD-6000 diffractometer (Bragg-Brentano geometry) equipped with a Cu K_α X-ray tube operated at 40 kV and 40 mA using a step size of 0.01° over the range 8-140° 2-theta. All specimens were spiked with a silicon standard (10 wt%, NIST660a, a = 5.40825 Å) to determine the unit cell constants absolutely using a full-pattern fitting method. Crystal structures were refined by Rietveld analysis using TOPAS 3[12].

The neutron powder diffraction (NPD) data were acquired at the Institute Laue-Langevin (ILL) Grenoble (France) using the high resolution D1A diffractometer with a wavelength of 1.389 Å, a 2-theta range of 0 – 150° and scan step size of 0.05° at room temperature. The diffractometer is equipped with a focusing Ge monochromator at a take-off angle of 123° and 25 standard ^{3}He counter detectors. A cylindrical sample container (0.9 cm diameter) was used during the measurement.

The structure refinements were carried out with TOPAS using a pseudo-Voigt peak shape profile (U = 0.12, V = -0.21, W = 0.17 as supplied by ILL) and a starting model using the atomic positions of $Ca_{10}(SiO_4)_3(SO_4)_3Cl_2$ in hexagonal $P6_3/m$[13]. Although monoclinic forms have been documented, such occurrences were not observed in this study, as 2*b* superstructure reflections were absent, and improvements in *R* values with lower symmetries ($P2_1/m$; $P2_1$) were insignificant. For each data set, a five-coefficient Chebychev function and $1/x$ background, a zero error, unit cell parameters, and crystal size were refined sequentially with temperature displacement parameters and occupation factors of each atomic site kept constant. Scattering lengths of 0.4700, 0.4149, 0.03521, 0.2847, 0.5803, and 0.9577 × 10^{-12} cm were used for Ca, Si, P, S, O, and Cl, respectively.[14] To ensure reasonable bond lengths in the SiO_4, PO_4, and SO_4 tetrahedra, fractional coordinates were constrained close to the average of the Si-O, P-O, and S-O bond lengths at 1.542 Å using a penalty function. After several refinement cycles, the calcium positions (Ca(1) and Ca(2)) were released, followed by the silicon/sulphur/phosphorus and oxygen positions. The oxygen sites were fully tenanted, while the occupancies of calcium and chlorine were allowed to vary. For nonstoichiometric ellestadites, the occupancy factors of Ca and Cl were constrained to maintain charge balance according to[15]

$$Ca^{2+} + 2\ Cl^- \rightarrow \square_{Ca} + 2\square_{Cl} \quad (2)$$

As the refinements do not suggest nonstoichiomety in the samples for $x \leq 1$, the standard occupancy factors (SOF) of Ca and the 4*e* Cl(1) + Cl(2) sum were fixed at SOF = 1 and SOF = 0.5 respectively. The mole ratio of Si:S at the tetrahedral site was 1:1 to maintain overall electrostatic neutrality in the crystal structure, and the sum of the occupancy of the Si/S/P was fixed to 6. Isotropic temperature displacement parameters for all atoms were refined in Ca(1)/Ca(2)/Cl and Si/P/S/O(1)/O(2)/O(3) groups to the same value. The refinement cycles were terminated when convergence was reached. Difference Fourier maps were generated using Jana2006[16] specifically to examine the location of anion scattering centers in the tunnels. To objectively assess the reliability of the Rietveld refinements singular value decomposition as implemented in SVDdiagnostic[17], was used to confirm the statistical robustness of the analysis (see supplementary information for detailed analysis).

2.4 Fourier-transform infrared (FTIR) spectroscopy

Infrared absorption spectra were recorded over the range 4000 - 400 cm^{-1} with a Fourier Transform Infrared Spectrometer (Perkin-Elmer Spectrum 2000). Ellestadite powders were prepared for FTIR measurement by manually grinding ca. 1 mg of powder in an agate mortar with pestle and dispersing though 200 mg of KBr. The homogenized mixture was pressed into 10-mm-diameter transparent pellets. Spectra were averaged over 32 scans with 2 cm^{-1} resolution, and background subtracted using a pure KBr pellet without the sample. Gaussian peaks were fitted to the FTIR with prominent shoulders modeled by the Fityk program[18].

2.5 Transmission electron microscopy (TEM)

Specimens were prepared by ultrasonically dispersing a small quantity of powder in acetone then placing a drop of suspension on a holey carbon-coated copper grid that was allowed to dry. High-resolution transmission electron microscopy (HRTEM) was carried out with a JEOL-2010 TEM (JEOL, Tokyo, Japan C_s = 0.5 mm and C_c = 1.1 mm) operated at 200 kV with a LaB_6 source. Samples were analyzed after orientation with a double tilting holder and the selected area electron diffraction (SAD) patterns recorded.

2.6 Leaching Test

The Toxicity Characterization Leaching Procedure (TCLP) of the Environmental Protection Agency (U.S. EPA, 1990) (EPA-SW 846 Method 1311)[19] was conducted on individual sintered pellets (10 mm diameter, ~1.4-1.5 g) to determine elemental losses of Ca. The leach solution was acetic acid (CH_3COOH) of pH 2.88 prepared by diluting 5.7 mL of glacial acid with deionized water to a volume of 1L. A liquid-to-solid mass (L/S) ratio of 20:1 (ml/g) was used and the time of extraction was 72 h. After the acetate buffer was added to the extractor bottle and the pellet was immersed in the solution with pH of 2.88 at the beginning of the extraction, the bottle was sealed and rotated at 300 rpm. After the leaching process, the leachants were filtered through 0.45 μm pore diameter membrane filters, and the pH determined immediately after collection. The samples were then protected from light and refrigerated at 4 °C (± 2 °C) prior to analysis. Element concentrations in the leachates were determined with an inductively coupled plasma optical emission spectrometer, Perkin-Elmer Model 3000 (ICP-OES). Quantitation was completed using manufacturer software and calibrated against nitric acid standard solutions. Four different calibration standard concentrations were used to cover the recommended linear range. Standards were prepared by serial dilution from 1000 ppm certified atomic absorption stock solutions. A set of three replicates was performed in each case, the precision of these measurements always being better than 4%.

3 Results and Discussion

3.1 Homogeneity of apatite

The phase purity of each sample was ascertained by quantitative powder XRD, with $CaSO_4$ appearing as a secondary phase for $0 \leq x \leq 3$, x in $Ca_{10}[(SiO_4)_x(PO_4)_{6-2x}(SO_4)_x]Cl_2$ (Fig. 2); mass balance requires other secondary phases, such as quartz, that were detected at levels too low for treatment by Rietveld refinement.

3.2 Infrared spectra

FTIR spectroscopy was used to study the interaction of phosphate substitutions with silicate and sulfate groups, where the systematic changes in atomic mass shift the wavenumber vibration and also modify the shape of the absorption bands. As the atomic masses of Si and S bracket that of P, the wavenumber of IR absorption will shift proportionally to confirm a solid solution has formed. Peak-fitted FT-IR spectra of apatite-ellestadite samples are shown in Fig. 3. Peak-fitting allowed the identification of individual tetrahedral groups and the estimation of their relative proportions. Comparing the spectra of pure chlorapatite and fully substituted ellestadite (Fig. 3, $x = 0$ and $x = 3$), the most notable effect of Si/S substitution are shifts in the BO_4 group bands between 1100 – 800 cm^{-1} and 700 – 500cm^{-1}. For chlorapatite ($x = 0$) the PO_4^{3-} groups v_3 mode appear 1046 and 1085 cm^{-1}, v_4 mode at 607 and 567 cm^{-1}; and v_1 mode at 961 cm^{-1}, consistent with the published values of Wilson[20], who reported infrared bands for hydroxyapatite at ~1090 and ~1050 cm^{-1} assigned to P-O anti-symmetric stretching vibration modes (v_3), vibrations at ~602 and ~570 cm^{-1} for O-P-O bending modes (v_4), and ~962 cm-1 for P-O symmetric modes (v_1). Spectra for pure ellestadite ($x = 3$) show prominent bands at approximately ~1137 and ~931 cm^{-1} attributable to v_3 stretching modes of the SO_4^{2-} and SiO_4^{4-} groups respectively. The doublet bands at 646 and 616 cm^{-1} are assigned to the v_4 bending mode of SO_4^{2-}, whereas doublet bands at 563 and 508 cm^{-1} are the v_4 bending mode of the SiO_4^{4-} group.[4] These changes are consistent with the "harmonic oscillator model" for the energy of IR-active vibrations, thus the wavenumber increases with increasing bond strengths and decreasing atomic masses. At intermediate compositions, the shape and intensity change progressively, and the phosphate mode v_3 at ~1046 cm^{-1} in $Ca_{10}(SiO_4)_{2.5}(PO_4)(SO_4)_{2.5}Cl_2$ becomes more intense with increasing phosphate content, while the bands of SO_4^{2-} and SiO_4^{4-} groups diminish. The partial, or very weak appearance, of absorption corresponding to the PO_4^{3-} v_1 (961 cm^{-1}) vibration in some samples (x = 2.5, 2, and 1.5, x in $Ca_{10}[(SiO_4)_x(PO_4)_{6-2x}(SO_4)_x]Cl_2$) is caused by the proximity of the PO_4^{3-} v_1 (961 cm^{-1}) and the SiO_4^{4-} v_3 (941 cm^{-1}) modes so that v_1 cannot be separated from the stronger v_3 absorption. Although the Rietveld refinements of XRD show anhydrite as the secondary phase in some compositions, the characteristic band of $CaSO_4$ at ~680 cm^{-1} is not detected in the FTIR spectra.[21] This may due to the low quantity of anhydrite in the samples. Table 1 collates the frequencies of IR absorption bands of the apatite-ellestadite solid solution.

According to Matthews[22], the carbonate ion will be expelled from the apatite structure at about 800 °C with the band-doublet at 1424 and 1456 cm^{-1} related to carbonate-apatite disappearing. As the synthesis temperature here is 950 °C, the existence of structural carbonate in ellestadite was precluded. The weak carbonate band observed at ~ 1415 and ~1450 cm^{-1} in samples x = 2.5, 2, 1.5 and 1, may be due to absorption of atmospheric CO_2 post synthesis. Treatment in dilute HCl acid[23] removes adsorbed carbonate and confirms that it is not bound crystallographically (see supplementary information section). A broad hydroxyl band from 2500 to 3500 cm^{-1} arises from atmospheric water adsorbed to the KBr specimen pellet, and removed by oven drying the KBr powder in oven at 300 °C. It is concluded, that to the limit of detection all the apatites are fully chlorinated.

Table 1. FT-infrared frequencies (cm^{-1}) and assignments for apatite-ellestadite solid solutions

vibration		x=3 ellestadite	x=2.5	x=2	x=1.5	x=1	x=0.5	x=0 apatite
SiO_4^{4-}	v_4	507	510	510	513	527		
		563	565	565	565	565	558	
	v_3	931 broad (796,902,962)	926 broad (857,910,954)	926 broad (877,919,953)	920 broad (916,950)	927 broad	927 broad	
SO_4^{2-}	v_4	616	620	610	624	643	636	
		646	644	646	645			
	v_3	1137 broad (1082,1137,1246)	1139 broad (1095,1146,1247)	1148 broad (1088,1148,1258)	1147 broad (1091,1147,1251)	1146 broad (1096,1166)	1142 broad (1092,1142)	
PO_4^{3-}	v_4				565	565	569	568
			608	605	608	608	607	607
	v_3		1036	1042	1046 broad	1044 broad (1011,1043)	1047 broad (1017,1045)	1046 broad (1040,1054)
				1088	1091	1088	1082	1084
	v_1					957	958	960

3.3 Crystal structure and refinements

The details of the crystal structure refinements including atomic positional parameters and atomic displacement parameters are given in Table 2, with selected atomic distances and bond angles collected in Table 3. Preliminary analysis of the X-ray diffraction patterns assumed the samples to be single-phase apatite. Inspection of the X-ray (Fig. 2) and neutron diffraction patterns (see supplementary information section) did not obviously indicate peak splitting or significant line broadening that might have led to a supposition of phase separation or lower symmetry.

To study the ordering of BO_4 tetrahedra in ellestadite, the $P2_1/m$ space group was used for the neutron data refinements. However, the similarity of neutron scattering lengths for Si, P, and S prevented successful occupancy refinement at the tetrahedral site. According to Sudarsanan[8], some degree of Si/S ordering in monoclinic hydroxylellestadite is evidenced by the three different sizes of the BO_4 tetrahedra. The average B-O bond distances are 1.57 Å and 1.52 Å respectively for Si and S tetrahedral sites, and 1.54 Å for the site with Si/S with 1:1

Table 2 Lattice parameters and crystallographic data for $Ca_{10}[(SiO_4)_x(PO_4)_{6-2x}(SO_4)_x]Cl_2$ from Rietveld refinements of powder neutron diffraction data*

Ellestaidte (wt%)		95.6(6)	97.6(2)	98.6(2)	95.7(6)	98.1(3)	100
$CaSO_4$ (wt%)		4.3(6)	2.3(2)	1.4(2)	4.2(6)	1.9(3)	--
nominal *x*		3	2.5	2	1	0.5	0
refined *x*		3	2.4	2.03	0.66	0.27	0
a (Å)		9.6691(3)	9.6622(3)	9.6537(5)	9.6257(4)	9.6299(2)	9.6182(1)
c (Å)		6.8531(3)	6.8438(2)	6.8354(4)	6.7892(3)	6.7833(2)	6.7920(1)
V ($Å^3$)		554.88(4)	553.32(4)	551.67(7)	544.77(5)	544.77(3)	544.15(2)
R_p		0.040	0.036	0.037	0.046	0.040	0.044
R_{wp}		0.052	0.047	0.048	0.059	0.052	0.056
R_{exp}		0.067	0.078	0.075	0.077	0.077	0.082
GOF**		0.77	0.59	0.64	0.77	0.67	0.69
R_b		0.032	0.028	0.022	0.021	0.022	0.029
Ca(1)	z	-0.0022(1)	-0.0027(9)	-0.003(1)	0.002(1)	0.0012(8)	-0.0009(6)
4*f*	Occ	0.9837(81)	0.9958(69)	0.9952(74)	1	1	1
	B	2.04(5)	1.91(4)	1.61(5)	1.02(4)	0.89(3)	0.87(3)
Ca(2)	x	0.2600(7)	0.2596(6)	0.2602(7)	0.2584(6)	0.2586(4)	0.2582(4)
6*h*	y	-0.0004(8)	-0.0008(7)	-0.0004(8)	0.0024(7)	0.0031(5)	0.0006(5)
	Occ	0.9830(53)	0.9754(44)	0.9753(48)	1	1	1
	B	2.04(5)	1.91(4)	1.61(5)	1.02(4)	0.89(3)	0.87(3)
P	x	0.4030(4)	0.4044(3)	0.4053(3)	0.4071(3)	0.4077(2)	0.4064(2)
6*h*	y	0.3728(4)	0.3739(3)	0.3746(3)	0.3750(3)	0.3752(2)	0.0.3740(2)
	Occ (Si)	0.5	0.40(1)	0.34(1)	0.11(1)	0.04(1)	
	Occ (S)	0.5	0.40(1)	0.34(1)	0.11(1)	0.04(1)	
	Occ (P)		0.20(2)	0.32(3)	0.78(3)	0.92(2)	1.00
	B	2.04(5)	2.14(3)	1.87(3)	1.12(3)	0.95(2)	1.05(2)
O(1)	x	0.3361(3)	0.3379(3)	0.3390(3)	0.3415(3)	0.3422(2)	0.3408(2)
6*h*	y	0.4880(3)	0.4894(3)	0.4898(3)	0.4918(3)	0.4917(2)	0.4906(2)
	B	2.20(3)	2.14(3)	1.87(3)	1.12(3)	0.95(2)	1.05(2)
O(2)	x	0.5886(3)	0.5895(3)	0.5903(4)	0.5919(3)	0.5925(2)	0.5913(2)
6*h*	y	0.4672(5)	0.4675(4)	0.4687(5)	0.4669(5)	0.4672(4)	0.4670(3)
	B	2.20(3)	2.14(3)	1.87(3)	1.12(3)	0.95(2)	1.05(2)
O(3)	x	0.3538(3)	0.3535(3)	0.3534(3)	0.3514(3)	0.3525(2)	0.3518(2)
12*i*	y	0.2665(3)	0.2667(2)	0.2668(3)	0.2664(3)	0.2665(2)	0.2653(2)
	z	0.0657(3)	0.0667(3)	0.0677(3)	0.0671(4)	0.0672(2)	0.0674(2)
	B	2.20(3)	2.14(3)	1.87(3)	1.12(3)	0.95(2)	1.05(2)
Cl(1)	z	0.425(1)	0.4290(9)	0.4308(1)	0.4388(1)	0.4418(8)	0.4343(8)
4*e*	Occ	0.416 (23)	0.418(192)	0.42(2)	0.4039(84)	0.4107(67)	0.3741(56)
	B	2.04(5)	1.91(4)	1.61(5)	1.02(4)	0.89(3)	0.87(3)
Cl(2)	z				0.154(5)	0.140(4)	0.153(3)
4*e*	Occ				0.0961(84)	0.0893(67)	0.1259(56)
	B				1.02(4)	0.89(3)	0.87(3)

*$R_p = (\Sigma_i|y_i-y_{ci}|)/\Sigma_i y_i$, $R_{wp} = [(\Sigma_i w|y_i-y_{ci}|^2)/\Sigma_i w|y_i|^2]^{1/2}$, $R_{exp} = [(\sum(M-P)/\sum w_m Y^2_{o,m}]^{1/2}$, GOF = $R_{wp}/R_{exp} = \Sigma_i w\,(y_i - y_{ci})^2/(n - p)$; ** The GOF <1 is a statistical artifact because the total counts are low (~2000 in the strongest peak) and the step size (0.05° 2θ) is large leading to an over estimation of R_{exp}.[24]

occupancy. In $P2_1/m$ the tetrahedrally coordinated atoms (Si/S) are divided among three 2-fold Wyckoff positions, however, refinement did not reveal such ordering, but rather the spread of B-O bond lengths in the crystallographically distinct BO_4 became non-physical (see supplementary information section). Therefore, refinements were carried in $P6_3/m$ and all tetrahedrally coordinated atoms are undifferentiated in a single 6-fold (6*h*) position (Table 3).

Fig. 4 shows that the relationship between the refined chemical compositions and unit cell parameters is almost linear from chlorellestadite to chlorapatite. Vegard's Law is therefore obeyed by this solid solution series. Both unit cell parameters *a* and *c* increased with the incorporation of silicon and sulphur. The effective size of PO_4 is slightly smaller than the average size of SiO_4 and SO_4, as seen from the variation of B-O bond lengths in Table 3. Thus, increasing the silicon and sulphur content dilates the unit cell. This result is consistent with the study of Rouse and Dunn[25], who described a solid solution series between ellestadite and calcium phosphate apatite. Those naturally occurring ellestadites containing F^- and OH^- instead of Cl^-, show a linear variation of lattice parameters when exchanging SiO_4^{4-} and SO_4^{2-} by $2PO_4^{3-}$.

A Ca-deficiency was found in x = 3, 2.5, and 2 compositions (Confirmed by electron probe microanalysis, see supplementary information for detailed analysis) with the loss of chlorine in the tunnel (Table 2), but Ca and Cl deficits were not observed for x = 1, 0.5, and 0; The $CaCl_2$ volatilization in ellestadite materials has been discussed in another paper[15]. Hounslow and Chao[26] studied the dependence of monoclinic character on chlorine content in mineral chlorapatite, and suggested that 10 to 15% of chlorine ions can be lost before the hexagonal form becomes evident by polarized light microscopy and X-ray diffraction. In our study, the atomic occupancies (Table 2) indicate that only about 80% of the stoichiometric amount of Cl is present in x = 3, 2.5, and 2 compositions, which eliminates the possibility of monoclinic ($P2_1/b$) chlorellestadite formation, since the loss of chlorine atoms removes the sterochemical driver for inter-tunnel chlorine ordering.

Difference Fourier maps (Fig. 5) of neutron scattering along the apatite tunnel show that across the ellestadite-apatite series the

chlorines occupy different positions. For x = 3, 2.5, and 2 compositions, there is only one Cl position z ≈ 0.43, and in x = 1, 0.5, and 0, a splitting of neutron scattering centres is evident. In synthetic $Mn_{10}(PO_4)_6Cl_2$ Engel et al.[27] explained a similar elongated electron density in the c direction and a slightly low chlorine occupancy by a 10% substitution of chlorine by OH ions. Our samples did not show OH bands in the infrared spectra. To investigate the positions of chlorines along the c axis, refinements and difference Fourier maps were prepared (i) without Cl^-, (ii) with one Cl^-, and (iii) two Cl^- for the compositions x = 1, 0.5, and 0. In pure apatite (x = 0) when there is only one chlorine (z = 0.429) in the tunnel, the difference Fourier map (Fig. 6) shows some remaining neutron scattering implying the possibility of multiple chlorine positions. By introducing a second Cl^- (z = 0.153), the difference Fourier map exhibits low neutron density residuals in the range of −0.85 e/Å^3 to 0.85 e/Å^3, and lower R-factors. Hence, difference maps show that, although most of the Cl ions are at the z ≈ 0.44 sites, some might be present at z ≈ 0.15 sites in the same tunnels. The environment of the chlorine ions is shown in Fig. 7. In the chlorellestadite (x = 3) structure, Cl ions are approximately in the center of an O(3) triangle (O(3)-O(3): 5.346(5)Å) in which the Cl-O(3) distances are 3.087(2) Å. With increasing phosphate content, the unit cell became smaller, and the O(3) triangle shrinks (O(3)-O(3) is 5.289(3) Å for chlorapatite, x = 0). To keep the average separation of O(3) and Cl reasonable, some of the Cl ions are displaced, from the center of the O(3) triangle towards to the Ca(2) triangle. The bond valences of Ca(1) and Ca(2) were calculated (Table 3), and no deficit of valence charge was found confirming the Rietveld refinements.

The CaO_6 metaprism twist angle (φ) can be used as a diagnostic tool to validate apatite structures and was calculated for all the compositions using the fractional coordinates of A(1), O(1) and O(2). For $P6_3/m$ apatite structures 5° < φ < 25° typically, and when the A(1) and A(2) are chemically identical, there is a linear relationship between φ and the average crystal radii regardless of whether substitution is made on the B or X sites. Broadly, the ellestadites fall into two groups – those that are stoichiometric with respect to chlorine (2 Cl per formula unit) and those sub-stoichiometric with less than two chlorines. Twist angle systematic predict that as chlorine is removed the tunnel will collapse and φ becomes larger. Fig. 9a compares the Ca(1)O_6 twist angle with the average effective atomic radius per unit cell that is consistent with the analysis[1] – when the tunnel chlorine sites are filled 18.1° ≤ φ ≤ 18.7°, but when the tunnel contains vacancies 19.2° ≤ φ ≤ 20.4°. If these two groups are studied in detail then the sub-stoichiometric group shows that a reduction of φ accompanies the in-filling of the tunnel with chlorine (Fig. 9b). For the stoichiometric group Si and S have a large average ionic than P, leading to greater tunnel and smaller φ. The observed value of φ (18.1°) for x = 0.5 is slightly below trend (Fig. 9c), and likely reflects the difficulty in refining chemically complex ellestadites, and the possibility of arriving at false minima using Rietveld refinements.

Table 3 Bond lengths (Å) and angles (°) for $Ca_{10}[(SiO_4)_x(PO_4)_{6-2x}(SO_4)_x]Cl_2$, and Bond-Valence Sums (BVS) of Ca(1) and Ca(2) sites

x	3	2.5	2	1	0.5	0
Ca(1)-O(1) × 3	2.453(5)	2.450(2)	2.449(5)	2.411(5)	2.416(4)	2.428(4)
Ca(1)-O(2) × 3	2.471(6)	2.463(5)	2.464(6)	2.453(6)	2.449(5)	2.444(4)
Ca(1)-O(3) × 3	2.793(4)	2.795(3)	2.794(4)	2.808(4)	2.800(3)	2.797(2)
twist angle (φ)	20.4(2)	19.8(1)	19.2(1)	18.4(1)	18.1(8)	18.7(7)
Ca(2)-O(2)	2.288(7)	2.287(4)	2.270(7)	2.294(7)	2.291(3)	2.293(4)
Ca(2)-O(3) × 2	2.331(4)	2.335(4)	2.341(3)	2.327(3)	2.332(3)	2.326(3)
Ca(2)-O(3) × 2	2.597(7)	2.595(6)	2.581(3)	2.554(3)	2.549(5)	2.557(4)
Ca(2)-Cl(1)	2.787(7)	2.795(7)	2.798(6)	2.788(7)	2.797(3)	2.778(5)
Ca(2)-Cl(2)				2.56(1)	2.585(8)	2.566(5)
O(3)-O(3)	5.346(5)	5.340(4)	5.335(5)	5.294(5)	5.310(3)	5.289(3)
O(3)-Cl(1)	3.087(2)	3.083(2)	3.080(3)	3.056(3)	3.066(2)	3.054(2)
O(3)-Cl(2)				3.114(3)	3.105(5)	3.108(4)
Ca(2)-Ca(2)	4.355(1)	4.351(1)	4.347(1)	4.288(1)	4.287(8)	4.295(7)
B-O(1)	1.542(6)	1.540(5)	1.536(5)	1.540(5)	1.536(4)	1.538(4)
B-O(2)	1.553(4)	1.549(4)	1.546(4)	1.541(4)	1.541(2)	1.540(2)
B-O(3) × 2	1.547(3)	1.542(3)	1.538(2)	1.537(3)	1.536(2)	1.535(2)
O(1)-B-O(2)	110.7(2)	110.8(2)	110.6(9)	110.9(3)	110.9(2)	110.6(2)
O(1)-B-O(3)	112.3(2)	112.2(2)	112.1(2)	111.5(2)	111.6(1)	111.7(1)
O(2)-B-O(3)	105.7(2)	106.2(2)	106.7(2)	107.5(2)	107.3(1)	107.4(9)
O(3)-B-O(3)	109.6(2)	108.8(2)	108.2(2)	107.7(2)	107.7(2)	107.8(2)
$Ca(1)_{BVS}$	1.98	1.99	1.94	2.00	2.04	2.00
$Ca(2)_{BVS}$	1.98	1.99	2.01	2.00	2.00	2.05

3.4 High resolution TEM

High-resolution TEM images of $Ca_{10}(SiO_4)_{1.5}(PO_4)_3(SO_4)_{1.5}Cl_2$ and $Ca_{10}(SiO_4)_{0.5}(PO_4)_5(SO_4)_{0.5}Cl_2$ show well developed crystals without obvious imperfections, in the sense that no extended defects are observed (Fig. 10). The intensity distribution of experimental SAD reflections (Fig. 11) was consistent with $P6_3/m$ symmetry. In a study of a Brazilian gem-grade apatite with a bulk composition of $(Ca_{3.948}Na_{0.052})Ca_{5.99}(P_{5.686}Si_{0.182}S_{0.132})O_{24}(F_{1.517}Cl_{0.120}OH_{0.363})$, Ferraris et al.[28] found some Si/S-rich crystals of ellestadite embedded in a host fluorapaite (F-Ap) and a guest chlorapatite (Cl-Ap). Such domains were not detected in any of our samples, with the thin ellestadite cyrstals appearing homogeneous. Similarly, the reduction of symmetry to $P2_1/m$ that was proposed earlier for $Ca_{10}(PO_4)_6Cl_2$ was not distinguishable by high-resolution imaging and diffraction.

3.5 Dissolution studies

TCLP test data, including weight loss, pH changes and Ca leachability are summarized in Table 4 and Fig. 12. The dissolution of ellestadite is congruent, followed by precipitation of insoluble salts. Based on the XRD analysis (Fig. 13) of the leached materials the primary dissolution and precipitation reactions are:

$$Ca_{10}[(SiO_4)_x(PO_4)_{6-2x}(SO_4)_x]Cl_2 + 20H^+ \rightarrow$$
$$10Ca^{2+} + xH_2SO_4 + xH_4SiO_4 + (6-2x)H_3PO_4 + 2HCl \quad (3)$$
$$Ca^{2+} + H_4SiO_4 \rightarrow CaSiO_3\,(s) + H_2O \quad (4)$$
$$CaSiO_3 + SO_4^{2-} + 2H^+ + 2H_2O \rightarrow CaSO_4{\cdot}2H_2O\,(s) + H_2SiO_3 \quad (5)$$
$$Ca^{2+} + SO_4^{2-} + H_2O \rightarrow CaSO_4{\cdot}2H_2O\,(s) \quad (6)$$
$$CaSiO_3 + 2CH_3CO_2H \rightarrow Ca^{2+} + 2CH_3CO_2^- + SiO_2\,(s) + H_2O \quad (7)$$

Table 4 Leachability* (concentration (M) and weight loss) of $Ca_{10}[(SiO_4)_x(PO_4)_{6-2x}(SO_4)_x]Cl_2$

x	pH**	Weight loss (%)	Ca (10^{-2}M)	Leachability in %
3	6.51	10.38	6.21	12.8
2.5	5.45	8.29	5.12	10.5
2	5.13	7.13	4.59	9.5
1.5	4.78	7.11	4.19	8.6
1	4.89	5.17	3.87	8.0
0.5	4.43	6.89	2.75	5.7
0	3.92	--	0.76	1.5

* Leach period: 72 hours;

Leachability = (weigh of Ca in leaching solution) /(weight of Ca in the pellet before leach test).

** The initial pH is 2.88 (glacial acid with deionized water)

With increasing substitution of Si/S for phosphorus, there is greater weight loss and the final pH is less acidic. The increase in pH may be attributed to basic SiO_4 ions that bind H^+ and release more free OH^- ions in solution. Dissolution becomes progressively evident in passing from the pure apatite end member towards the pure ellestadite end member; leachability increases with the increasing of Si/S content.

There are two possible explanations for the higher solubility of ellestadite compared to phosphate apatite. (1) As described by Gupta et al.[30] differences in the Gibbs free energy for hydration ΔG_{hi} versus the lattice $\Delta G_{lattice}$ change the Gibbs free energy energy of dissolution ΔG_{soln} such that $\Delta G_{soln} = \Sigma\Delta G_{hi} - \Delta G_{lattice}$. As the lattice expands, $\Delta G_{lattice}$ also becomes larger and solubility increases, and is particularly important where there is large different in the size of the anionic tetrahedrally co-ordinated cations; so for example, vanadate VO_4^{3-} apatites (IR V^{5+} = 0.35 Å) have an expanded lattice compared to phosphate PO_4^{3-} apatites (IR P^{5+} = 0.15 Å) and consequently are more soluble. However, in the case of ellestadites, this mechanism is not dominant as the lattice parameters change modestly with composition (see Table 2) because the $Si^{4+} + S^{6+}$ average ionic radii is almost equal to that of P^{5+}. (2) The second, and correct explanation, put forward by Leshkivich and Monroe[31], is that smaller free energies of formation correspond to higher solubility. These workers compared ΔG_f for apatite $Ca_{10}(PO_4)_6F_2$ (-6755 kJ.mol^{-1}) with ellestadite $Ca_{10}(SiO_4)_3(SO_4)_3F_2$ (-5760 kJ.mol^{-1}) and found these to be consistent with the higher solubility of the latter. In addition, the decomposition temperature of $Ca_{10}(PO_4)_6Cl_2$ (1300°C) is higher than $Ca_{10}(SiO_4)_3(SO_4)_3Cl_2$ (1000°C) and this is also consistent with a higher ΔG_f.

Here we observe increasing dissolution of apatite as Si + S progressively replaces P, with a significant change in solubility, and therefore ΔG_f, for the composition x = 1 in $Ca_{10}[(SiO_4)_x(PO_4)_{6-2x}(SO_4)_x]Cl_2$ (Fig. 12). It is evident that ellestadites with $x \leq 1$ in $Ca_{10}[(SiO_4)_x(PO_4)_{6-2x}(SO_4)_x]Cl_2$ are most chemically resistant to TCLP extractions, and are preferred for waste immobilization of silicon and sulphur rich wastes.

Conclusions

X-ray and neutron diffraction data analysis found all ellestadites $Ca_{10}[(SiO_4)_x(PO_4)_{6-2x}(SO_4)_x]Cl_2$ synthesized by short duration (9 hours) heat treatment are $P6_3/m$ and show no evidence of Si/P/S ordering at the tetrahedral sites. In detail, there are calcium and chlorine deficiencies in the Si/S rich compositions ($3 \leq x \leq 2$) due to the evaporation of $CaCl_2$ during the synthesis. For $x \leq 1.5$ where the Ca and Cl sites are fully occupied, a second low occupancy Cl site appears to reduce steric repulsion with the O(3) triangles.

Leaching tests show that phosphated ellestadites have superior chemical stability when the atomic proportion of phosphorus replaced by silicon and sulphur does not exceed one-third. For intractable solid wastes that are rich in silicon and/or sulphur together with toxic metals including lead, cadmium, and chromium, immobilization may be an alternative to direct stabilization in concrete which leads to substantial bulking, or disposal in secure landfills. Large toxic metals can replace Ca and smaller metals can replace Si/P/S in ellestadites according to crystallochemical principles, e.g.

$Ca^{2+} \rightarrow Pb^{2+}$ (9)

$S^{6+} + Si^{4+} \rightarrow 2Cr^{5+}$ (10)

$Ca^{2+} + S^{6+} + Si^{4+} \rightarrow Cd^{2+} + 2V^{5+}$ (11)

$Na^{+} + S^{6+} \rightarrow Pb^{2+} + P^{5+}$ (12)

This investigation suggests that incinerator fly ashes, containing difficult to stabilize sulphur and halides, can be fixed at moderate waste loadings in chemically tailored ellestadites. Such waste forms may permit re-use as aggregate in non-structural concrete applications.

Acknowledgements

We acknowledge Nanyang Technological University, Singapore, for the NTU Research Scholarship supporting this study.

Notes and references

[a] School of Materials Science & Engineering, Nanyang Technological University, 50 Nanyang Avenue, 639798, Singapore. E-mail: YNFANG@ntu.edu.sg, tjwhite@ntu.edu.sg .

[b] Energy Research Institute @ NTU (ERI@N), Research Technoplaza, Nanyang Technological University, Nanyang Drive, 637553, Singapore.

[c] Institut Laue-Langevin, 6 rue Jules Horowitz, 38042 Grenoble Cedex 9, France.

Electronic Supplementary Information (ESI) available: [Neutron crystallographic files in CIF format; examples of the output of *SVDdiagnostic* of Rietveld refinements of ellestadites; bond lengths of refined monoclinic structures; data of electron probe microanalysis; FTIR spectra of HCl washed samples; experimental and calculated neutron diffraction patterns]. See DOI: 10.1039/b000000x/

1 T. J. White, C. Ferraris, J. Kim and S. Madhavi, *Rev. Mineral. Geochem.*, 2005, **57**, 307.

2 Z. Dong, T. J. White, B. Wei and K. J. Laursen, *J. Am. Ceram. Soc.*, 2002, **85**, 2515-2522.

3 B. L. Metcalfe, I. W. Donald, S. K. Fong, L. A. Gerrard, D. M. Strachan, R. D. Scheele, *J. of Nucl. Mater.*, 2009, **385**, 485-488.

4 J. Neubauer and H. Pöllmann, *N. Jb. Miner. Abh.*, 1995, **168(3)**, 237-258.

5 D. McConnell, *Am. Mineral.*,1937, **22**, 977-986.

6 Y. Pliego-Cuervo and F. P. Glasser, *Cement Concr. Res.*, 1978, **8**, 519-524.

7 J. Neubauer and H. Pöllmann, *N. Jb. Miner. Abh.*, 1992, **7**, 295-310.

8 K. Sudarsanan, *Acta. Cryst. B: Struct. Sci.*, 1980, **36**, 1636-1639.
9 J. C. Elliot, P. E. Mackie, and R. A. Young, *Science*, 1973, **180**, 1055-1057.
10 N. I. Organova, R. K. Rastsvetaeva, O. V. Kuz'mina, G. A. Arapova, M. A. Litsarev and V. I. Fin'ko, *Kristallografiya*, 1994, **39**, 278-282.
11 J. C. Stormer, M. L. Pierson, and R. C. Tacker, *American Mineralogist*, 1993, **78**, 641-648.
12 Bruker. TOPAS Version3, Bruker AXS Inc., Madison, WI, USA, 25005.
13 S. J. Saint-Jean, E. JØns, N. Lundgaard and S. Hansen, *Cem. Concr. Res.*, 2005, **35**, 431-437.
14 V. F. Sears, *International Tables for Crystallography*, A. J. C. Wilson, Ed., Kluwer Academic Publishers: Dordrecht, 1993, **Vol C**, 383.
15 Y. N. Fang, C, Ritter, and T. White, *Inorg. Chem.*, 2011, **50**, 12641-12650.
16 V. Petricek, M. Dusek, L. Palatinus, *Jana2006, The Crystallographic Computing System*, Institute of Physics: Praha, Czech Republic, 2006
17 (25) P. H. J. Mercier, Y. Le Page, P. S. Whitfield, and L. D. Mitchell, *J. Appl. Crystallogr.* 2006, **39**, 458−465.
18 M. Wojdyr, *J. Appl. Cryst*. 2010, **43**, 1126-1128
19 U. S. EPA, Part 261, *Appendix II-Method 1311 Toxicity characteristic leaching procedure (TCLP), Federal Register, vol 55, no. 61, 1990, Rules and Regulations*, 1990, 11863-11877.
20 H. Morgan, R. M. Wilson, J. C. Elliott, S. E. P. Dowker, and P. Anderson, *Biomaterials*, 2000, **21**, 617-627.
21 K. Tonsuaadu, M. Peld, M. Quarton, et al., *Phosphorus, Sulfur, and Silicon and the Related Elements*, 2002, **177**, 1873-1876.
22 A. Matthews, Y. Nathan, *Am. Mineral.,* 1977, **62**, 565-573.
23 S. Madhavi, C. Ferraris, T. J. White, *J. Solid. State. Chem*., 2005, **178**, 2838-2845.
24 L. B. McCusker, R. B. Von Dreele, D. E. Cox, D. Louër and P. Scardi, *J. Appl. Crystallogr.* , 1999, 32:36-50.
25 R. C. Rouse and R. J. Dunn, *Am. Mineral*., 1982, **67**, 90-96.
26 A. W. Hounslow and G. Y. Chao, *Canad. Miner*., 1970, **10**, 252-259.
27 G. Engel, J. Pretzsch, V. Gramlich, and W. H. Baur, *Acta Crystl.*, 1975, **B31**, 1854-1860.
28 C. Ferraris; T. J. White, J. Plévert, R. Wegner,. *Phys. Chem. Mineral*, 2005, **32**, 485-492.
29 Klaus Brandenburg, Diamond Version 3, Crystal Impact GbR, Bonn, Germany.
30 K. S. Leshkivich and E. A. Monroe, *J. Mater. Sci*., 1993, **28**, 9-14.
31 Sudhir K. Gupta, P. V. R. Rao, G. George, and T. S. B. Narasaraju, *J. Mater. Sci*., 1987, **22**, 1286-1290.

List of Figures：

Fig. 1 Hexagonal $P6_3/m$ ellestadite structure of $A_{10}(BO_4)_6X_2$. The AO_6 metraprisms contain calcium, while the BO_4 tetrahedra accommodate phosphorus, sulfur and silicon. The tunnel position centred at the origin may contain halides or oxygen.

Fig. 2 Experimental X-ray diffraction data (line) and Rietveld fit (solid dots) of the synthetic chlorellestadite ($Ca_{10}[(SiO_4)_x(PO_4)_{6-2x}(SO_4)_x]Cl_2$): (a) x = 3, (b) x = 1.0, (c) x = 0, heated in air at 950 °C.

Fig. 3 Peak-fitted FT-IR spectra of apatite-ellestadite solid solutions. Sample labels indicate x in $Ca_{10}[(SiO_4)_x(PO_4)_{6-2x}(SO_4)_x]Cl_2$.

Fig. 4 Unit cell parameters (a and c) and cell volume (V) derived from Reitveld refinements of XRD (black square) and neutron (red dot) data as a function of the phosphorus content. Errors are within the size of the symbols.

Fig. 5 Difference Fourier maps of $Ca_{10}[(SiO_4)_x(PO_4)_{6-2x}(SO_4)_x]Cl_2$ ellestadites tunnel indicating the positions of Cl ions that were excluded to emphasize their location.

Fig. 6 Difference Fourier maps of neutron scattering with no Cl^-, one Cl^- (z = 0.429) and two Cl^- (z = 0.434 and 0.153) sites in the apatite ($Ca_{10}(PO_4)_6Cl_2$) tunnel. Contour interval is 0.2 e/Å^3 and the first positive contour (solid line) is at 0.2 e/Å^3. Negative difference nuclear density is indicated by the broken contours.

Fig. 7 Chirographic view of the chlorine ion environment and difference Fourier maps before and after including Cl ions in the tunnel, (a) $Ca_{10}(SiO_4)_3(SO_4)_3Cl_2$ and (b) Ca_{10} $(PO_4)_6Cl_2$. The sphere radii represent isotropic thermal displacements. Contour interval is 0.2 e/Å^3 and the first

positive contour (solid line) is at 0.2 e/Å^3. Negative difference nuclear density is indicated by the broken contours. The plot was prepared by Diamond[29].

Fig. 8 Correlation of composition and metaprism twist angle (φ). Errors are within the size of the symbols.

Fig. 9 Trends in metaprism twist angel for $Ca_{10}[(SiO_4)_x(PO_4)_{6-2x}(SO_4)_x]Cl_2$ as a function of (a) average effective ionic radius for the whole unit cell contents, (b) chlorine content in per formula unit, and (c) average effective B-Cation radius.

Fig. 10 HRTEM images taken from [001] zone axis of (a) $Ca_{10}(SiO_4)_{1.5}(PO_4)_3(SO_4)_{1.5}Cl_2$ and (b) $Ca_{10}(SiO_4)_{0.5}(PO_4)_5(SO_4)_{0.5}Cl_2$ ellestadite.

Fig. 11 SAD pattern taken from [001] zone axis of (a) $Ca_{10}(SiO_4)_3(SO_4)_3Cl_2$ and (b) $Ca_{10}(SiO_4)_2(PO_4)_2(SO_4)_2Cl_2$. No diffuse intensity or split reflections are present.

Fig. 12 Leachability of ellesadite in acetic acid and concentration of Ca in the leaching solution. The preferred compositional range for ellestadite waste forms is shaded.

Fig. 13 Representative X-ray diffraction profile of $Ca_{10}(SiO_4)_3(SO_4)_3Cl_2$ (a) before and (b) after leaching test.

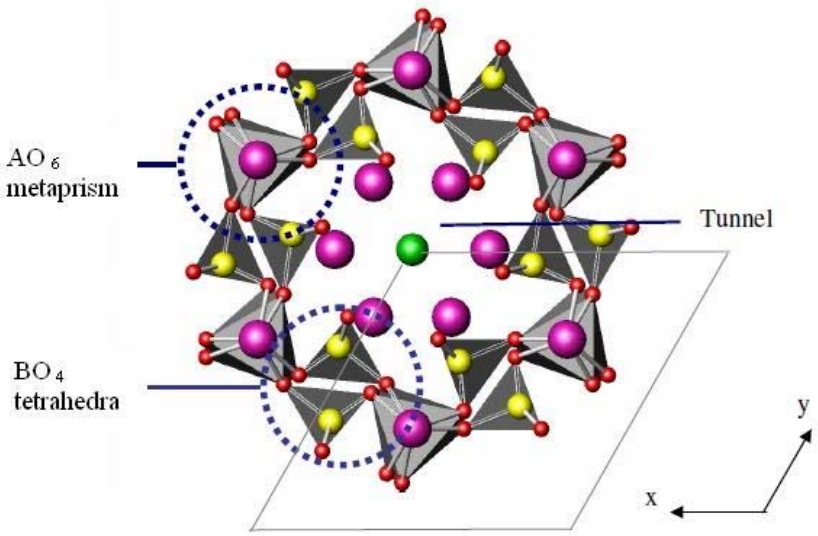

Fig. 1 Hexagonal $P6_3/m$ ellestadite structure of $A_{10}(BO_4)_6X_2$. The AO_6 metaprisms contain calcium, while the BO_4 tetrahedra accommodate phosphorus, sulfur and silicon. The tunnel position centred at the origin may contain halides or oxygen.

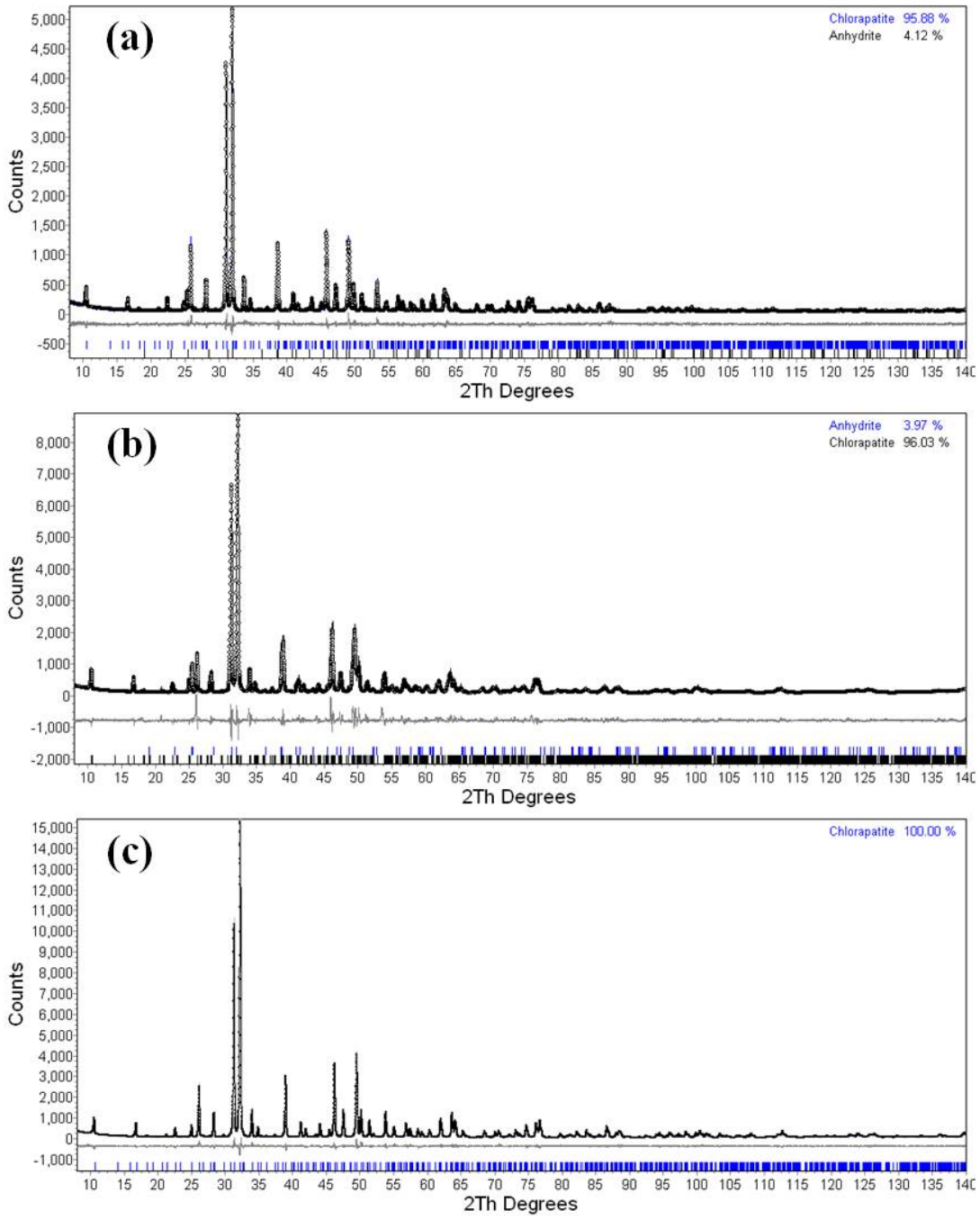

Fig. 2 Experimental X-ray diffraction data (line) and Rietveld fit (solid dots) of the synthetic chlorellestadite ($Ca_{10}[(SiO_4)_x(PO_4)_{6-2x}(SO_4)_x]Cl_2$): (a) $x = 3$, (b) $x = 1.0$, (c) $x = 0$, heated in air at 950℃.

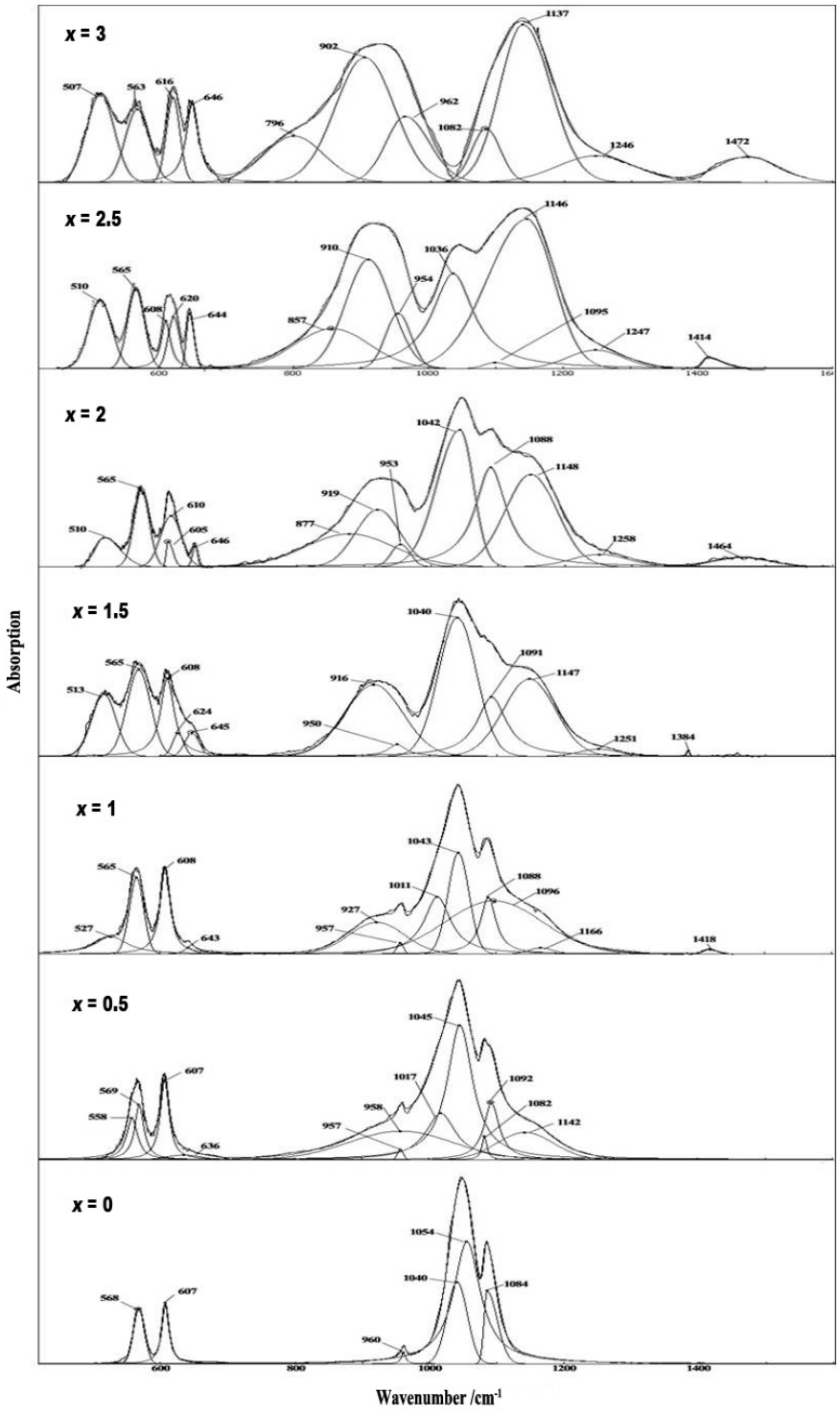

Fig. 3 Peak-fitted FT-IR spectra of apatite-ellestadite solid solutions. Sample labels indicate x in $Ca_{10}[(SiO_4)_x(PO_4)_{6-2x}(SO_4)_x]Cl_2$.

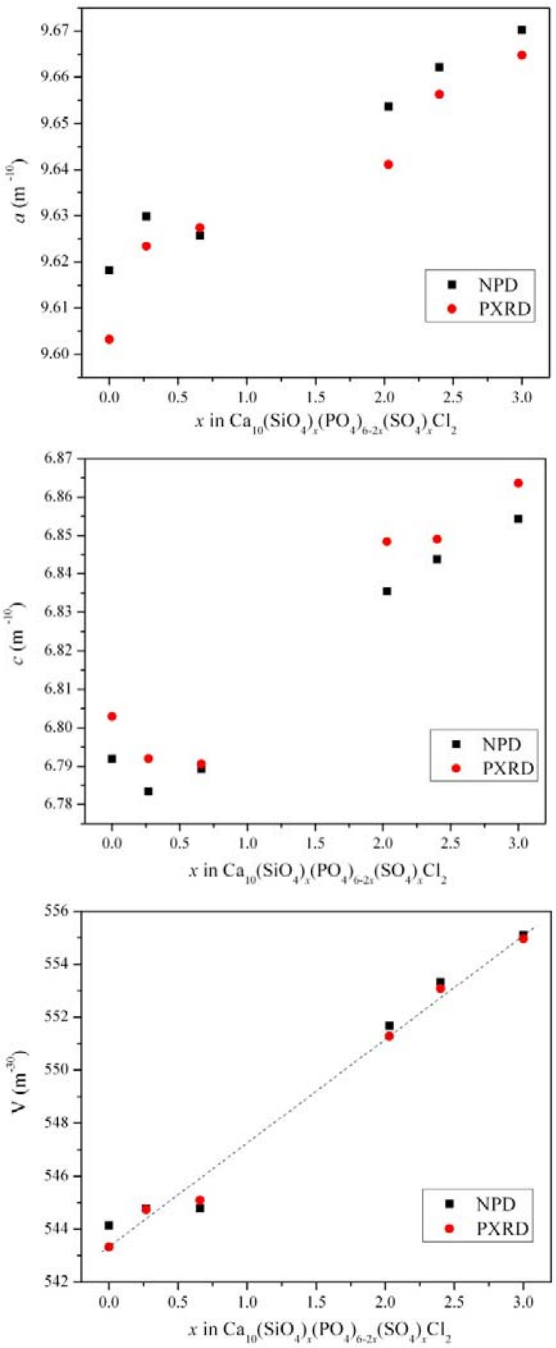

Fig. 4 Unit cell parameters (*a* and *c*) and cell volume (V) derived from Reitveld refinements of XRD (black square) and neutron (red dot) data as a function of the phosphorus content. Errors are within the size of the symbols.

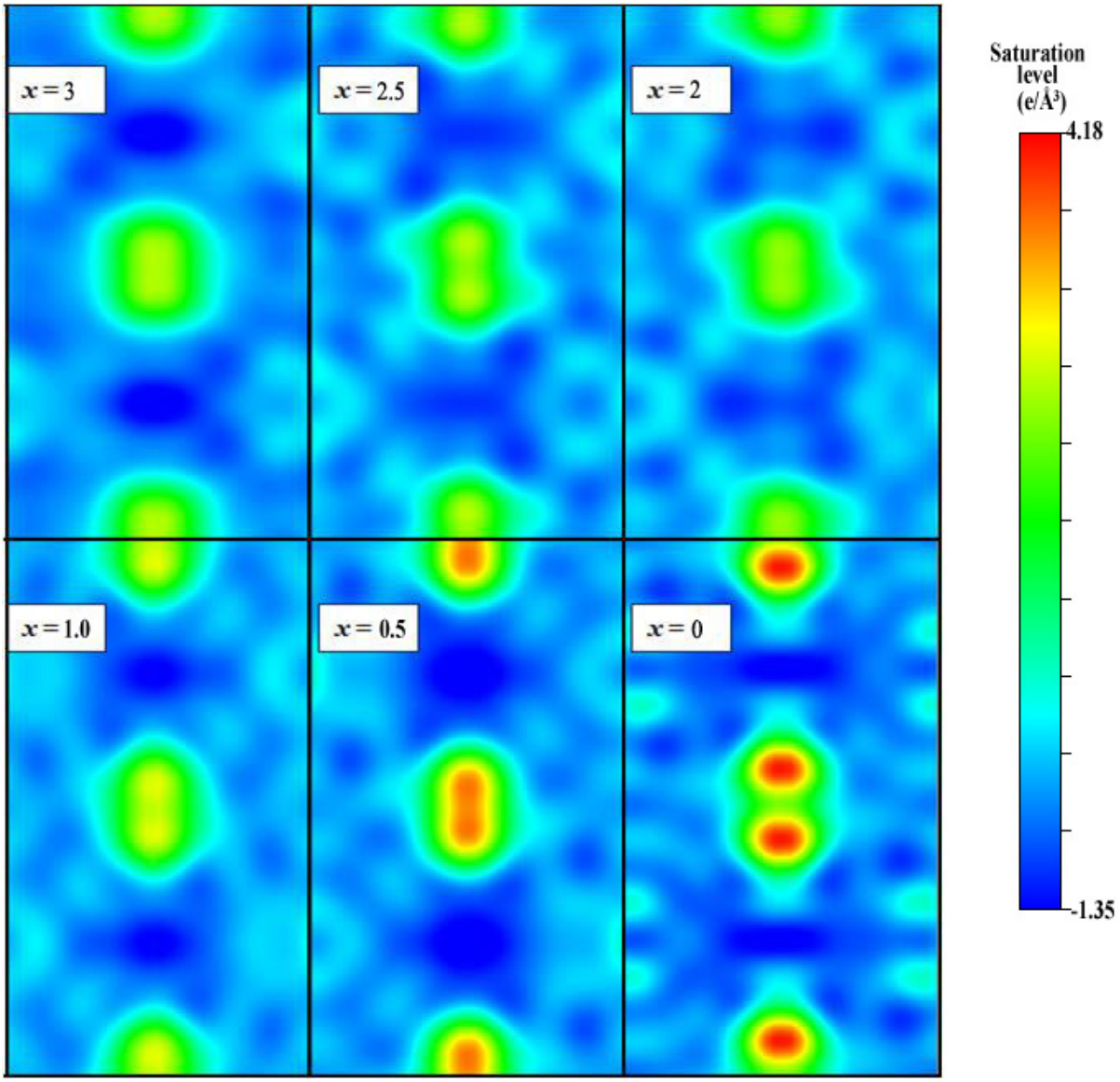

Fig. 5 **2D** Difference Fourier maps of $Ca_{10}[(SiO_4)_x(PO_4)_{6-2x}(SO_4)_x]Cl_2$ ellestadites tunnel indicating the positions of Cl ions that were excluded to emphasize their location. The saturation level range is from -1.35 e/Å^3 to 4.18 e/Å^3.

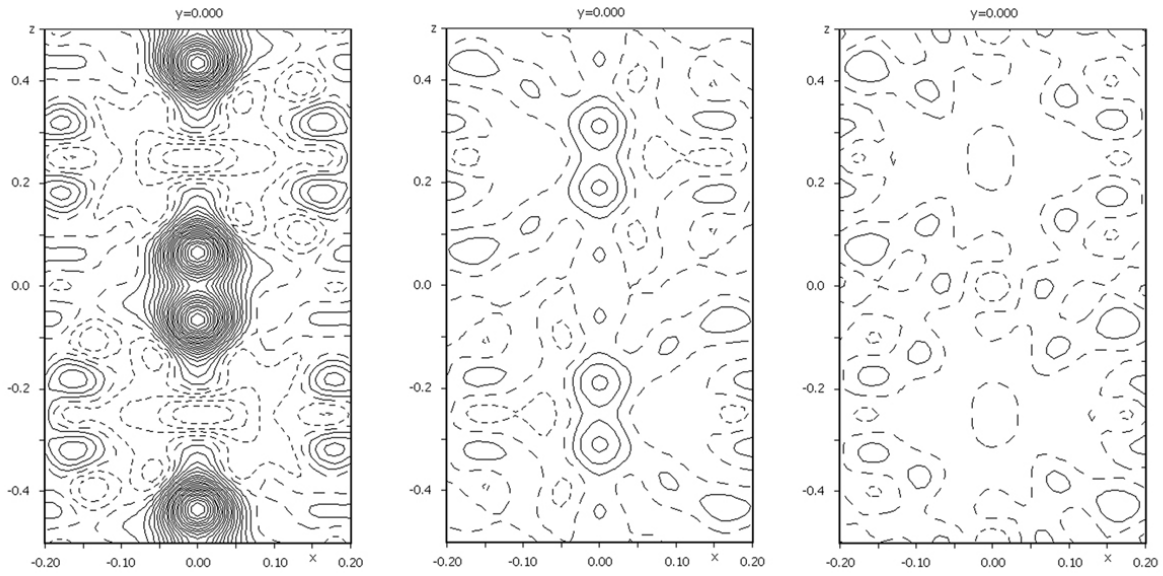

Fig. 6 Difference Fourier maps of neutron scattering with no Cl^- , one Cl^- (z = 0.429) and two Cl^- (z = 0.434 and 0.153) sites in the apatite ($Ca_{10}(PO_4)_6Cl_2$) tunnel. Contour interval is 0.2 e/Å^3 and the first positive contour (solid line) is at 0.2 e/Å^3. Negative difference nuclear density is indicated by the broken contours.

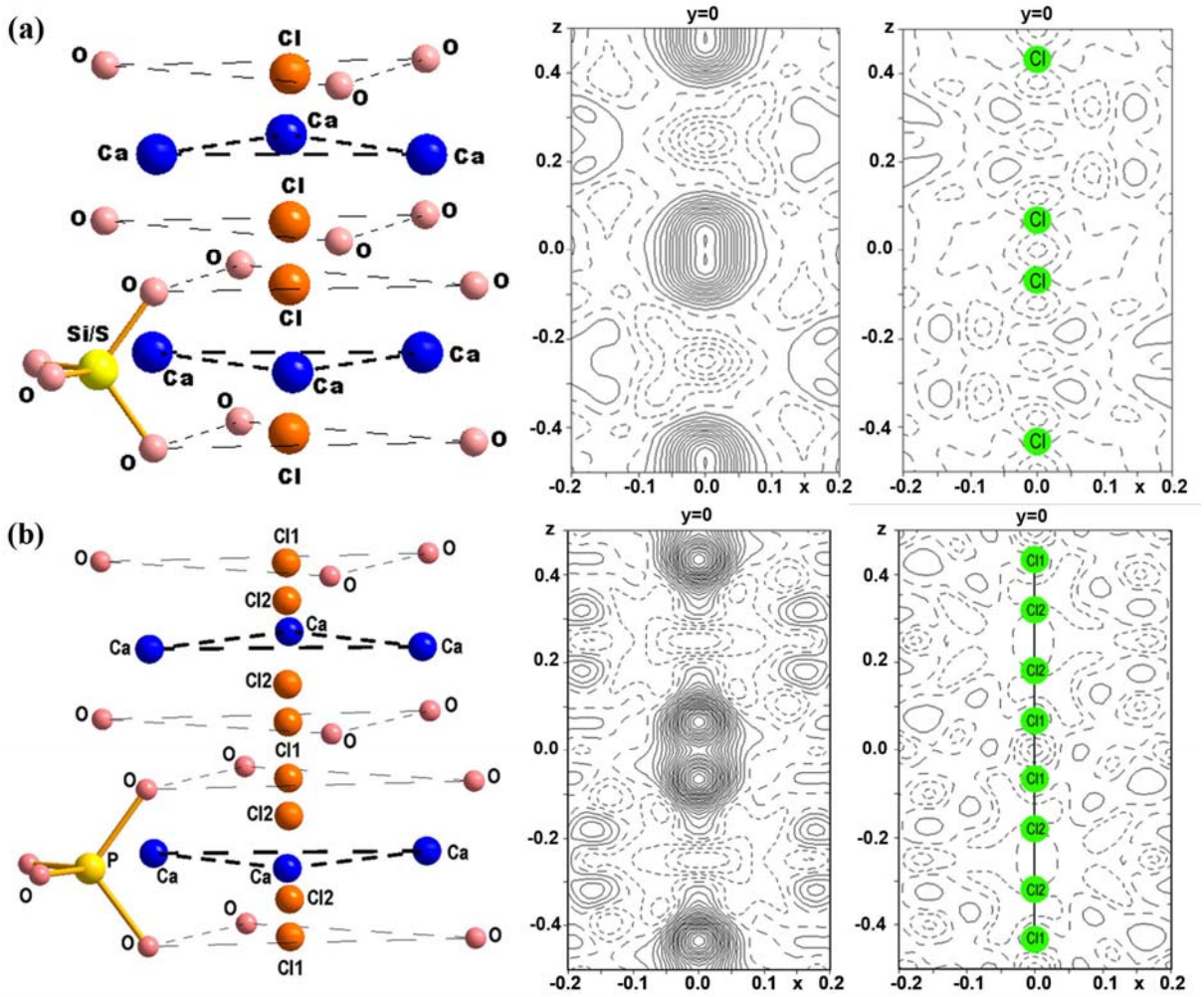

Fig. 7 Chirographic view of the chlorine ion environment and difference Fourier maps before and after including Cl ions in the tunnel, (a) $Ca_{10}(SiO_4)_3(SO_4)_3Cl_2$ and (b) $Ca_{10}(PO_4)_6Cl_2$. The sphere radii represent isotropic thermal displacements. Contour interval is 0.2 e/Å^3 and the first positive contour (solid line) is at 0.2 e/Å^3. Negative difference nuclear density is indicated by the broken contours. The plot was prepared by Diamond[29].

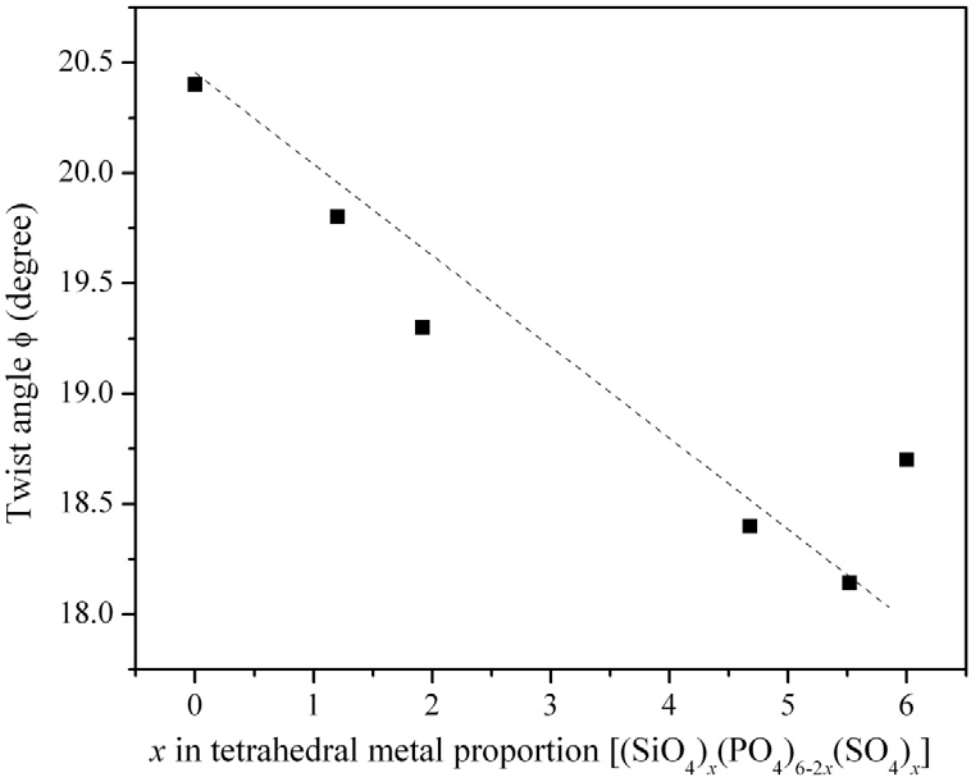

Fig. 8 Correlation of composition and metaprism twist angle (φ). Errors are within the size of the symbols.

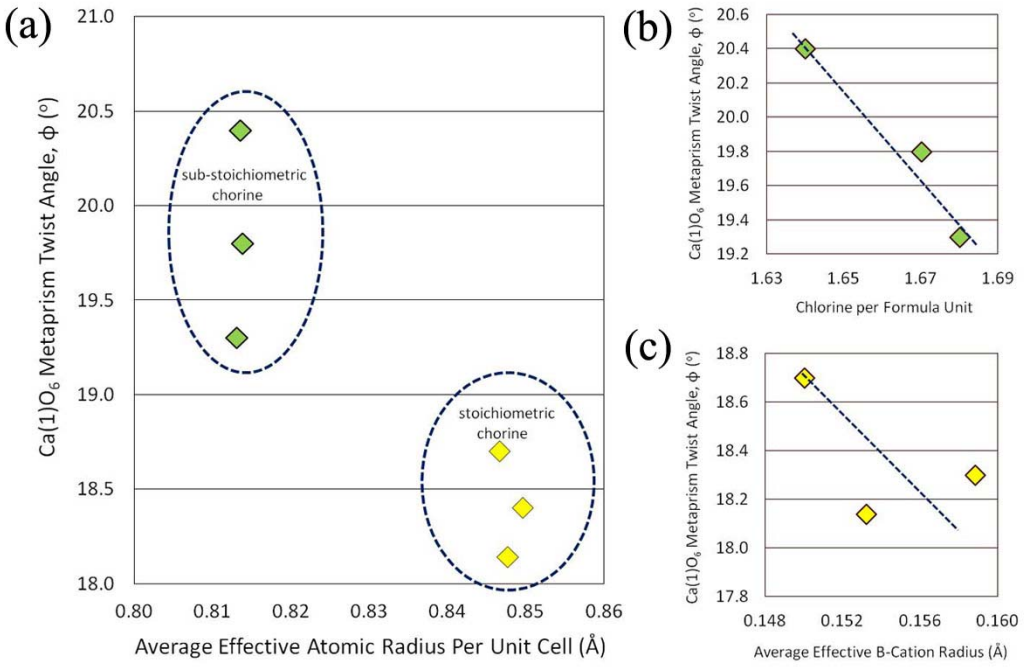

Fig. 9 Trends in metaprism twist angel for $Ca_{10}[(SiO_4)_x(PO_4)_{6-2x}(SO_4)_x]Cl_2$ as a function of (a) average effective ionic radius for the whole unit cell contents, (b) chlorine content in per formula unit, and (c) average effective B-Cation radius.

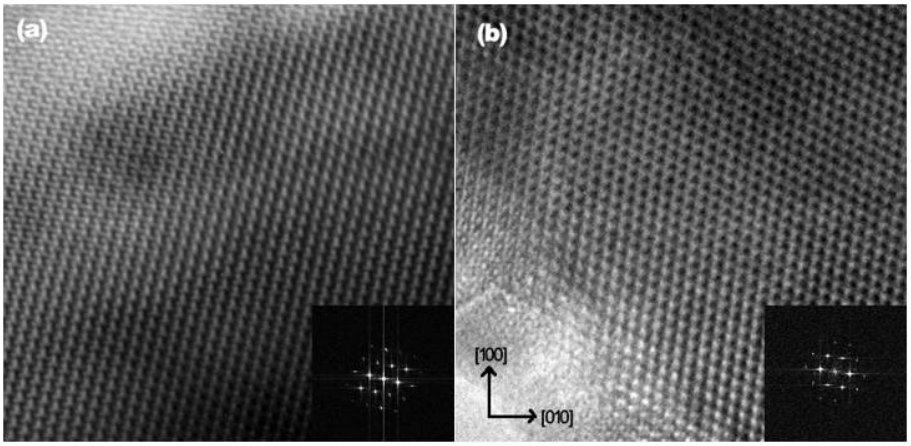

Fig. 10 HRTEM images taken from [001] zone axis of (a) $Ca_{10}(SiO_4)_{1.5}(PO_4)_3(SO_4)_{1.5}Cl_2$ and (b) $Ca_{10}(SiO_4)_{0.5}(PO_4)_5(SO_4)_{0.5}Cl_2$ ellestadite.

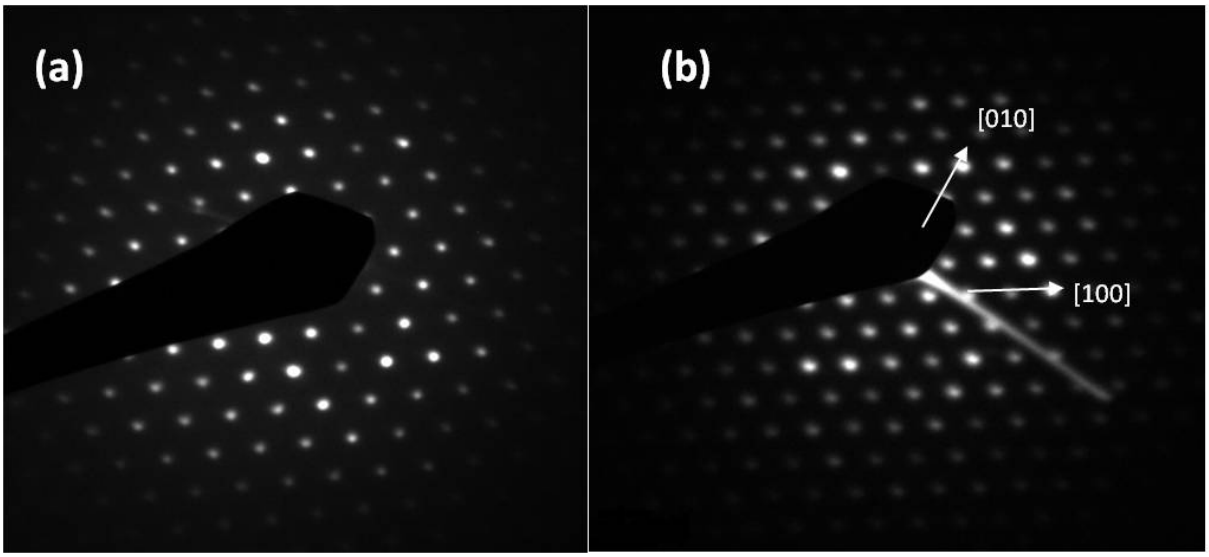

Fig. 11 SAD pattern taken from [001] zone axis of (a) $Ca_{10}(SiO_4)_3(SO_4)_3Cl_2$ and (b) $Ca_{10}(SiO_4)_2(PO_4)_2(SO_4)_2Cl_2$. No diffuse intensity or split reflections are present.

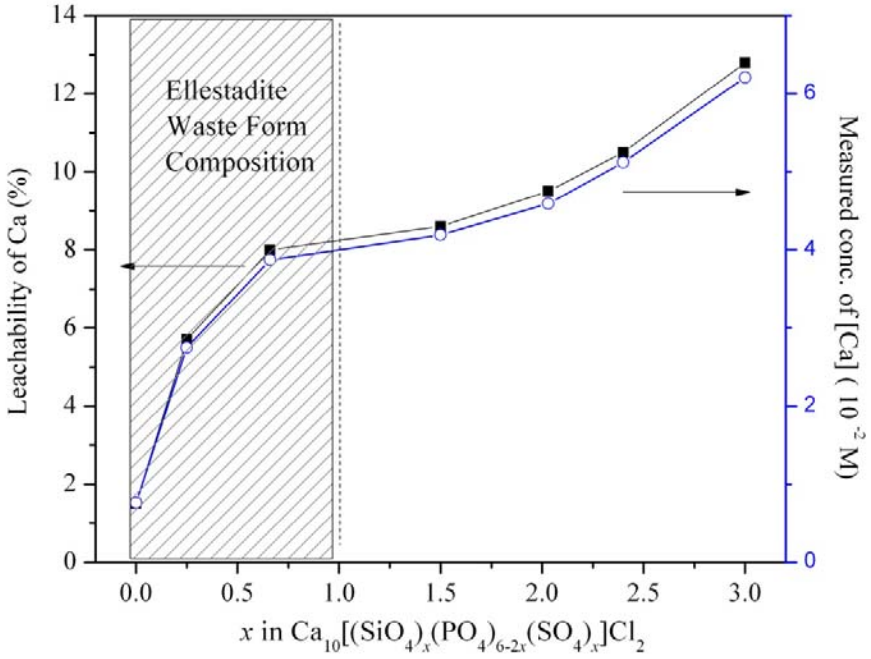

Fig. 12 Leachability of ellesadite in acetic acid and concentration of Ca in the leaching solution. The preferred compositional range for ellestadite waste forms is shaded.

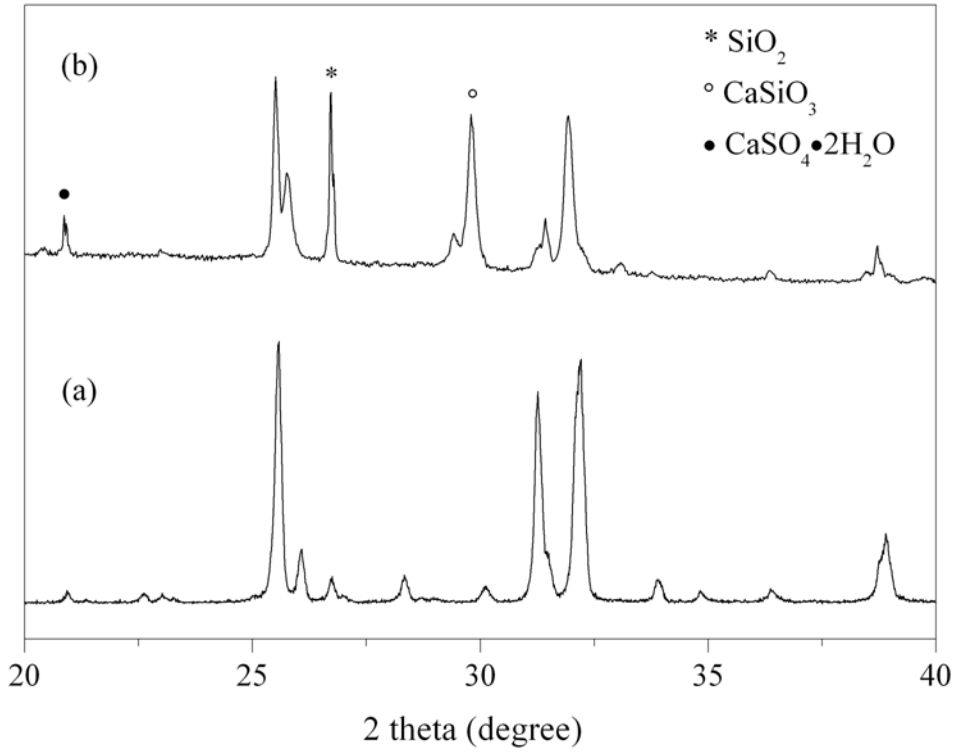

Fig. 13 Representative X-ray diffraction profile of $Ca_{10}(SiO_4)_3(SO_4)_3Cl_2$ (a) before and (b) after leaching test.